Dynamic formulation of phase field fracture in heterogeneous media with finite thickness cohesive interfaces

Mauro Corrado[a,*], Marco Paggi[b], José Reinoso[c]

[a] *Department of Structural, Geotechnical and Building Engineering, Politecnico di Torino, Corso Duca degli Abruzzi 24, 10129 Torino, Italy*
[b] *IMT School for Advanced Studies Lucca, Piazza San Francesco 19, 55100 Lucca, Italy*
[c] *School of Engineering, Universidad de Sevilla, Camino de los Descubrimientos s/n, 41092 Seville, Spain*

Abstract

Robust numerical prediction of crack propagation in heterogeneous media has been a matter of relevant importance in many engineering applications. In this study, a modelling framework for triggering dynamic fracture events in heterogeneous media, like layered materials, with internal finite thickness cohesive interfaces is proposed through the exploitation of the combined use of the phase field approach to fracture and the interface cohesive zone model to simulate the interplay between bulk and interface cracking. The proposed formulation is constructed via a consistent variational formalism leading to a coupled system of equations, which are solved using a staggered solution scheme. Representative applications examine the robustness of the computational approach, exhibiting results consistent with experimental evidences available in the literature.

Keywords: Nonlinear fracture mechanics; Dynamics; Finite thickness interfaces; Phase Field fracture

1. Introduction

The landmark research conducted by Francfort and Marigo [1] revisiting the foundations of the Griffith's vision of brittle fracture has promoted the advent

*Corresponding author
Email address: mauro.corrado@polito.it (Mauro Corrado)

of a new paradigm for the numerical modelling of cracking events in solids and structures. Subsequent developments on this matter recalled this variational viewpoint for the comprehensive formulation of new fracture models, being denominated as Phase Field (PF) models of fracture, which emerged through the consistent exploitation of Γ-convergence [2]. Taking as baseline the variational formalism of the formulation given in [1], notable research efforts have been carried out for the corresponding numerical framework and the subsequent computational implementation, leading to different families of PF approaches to fracture, such as the regularized variational formulation proposed by Bourdin and co-authors [2, 3] and the thermodynamic consistent approximation advocated by Miehe et al. [4] introducing a state-dependent variable (the maximum of the elastic energy) in order to prevent the material healing, among many others.

This renovated interest for predictive fracture methods relying on a smeared crack representation has been motivated by the inherent characteristics of PF formulation, which efficiently accounts for complex cracking patterns including intersections, branching, among many other different scenarios. PF methods inherently hold several appealing aspects such as the ability for the automatic crack tracking and crack nucleation, the versatility to accommodate different constitutive models. This potential prompted that PF methods have garnered a great deal of research attention in the last decade, including the corresponding extensions for ductile fracture [5, 6], hydrogen-assisted cracking [7], fibre-reinforced composites at different length scales [8, 9], polycrystalline materials [10] and alternative formulations for PF methods [11].

Moreover, this computational technique for fracture has been also extended to model dynamic fracture in solids [12, 13, 14, 15, 16, 17], following analogous assumptions as for nonlocal damage formulations in dynamics, pinpointing again the inherent versatility of the method, although mainly focused to homogeneous material systems and solids. However, in real materials and structures heterogeneities and inclusions in conjunction with different constituents separated by interfaces or thin adhesive layers are ubiquitous. Stemming from these aspects,

the authors recently proposed a modeling framework exploiting the combined use of PF and cohesive zone model (CZM) techniques in statics, in order to account for bulk and interface fracture events, respectively, in a consistent and efficient manner [18, 10]. In this concern, the present investigation is devoted to formulate a consistent extension of the PF-CZM technique to dynamic fracture events in heterogeneous systems, following the main developments outlined in [19, 20].

2. Dynamic Phase Field formulation for heterogeneous systems including finite thickness interfaces

2.1. Fundamentals of the combined phase field and cohesive-like fracture modelling for heterogeneous media

This section briefly introduces the main aspects of the phase field (PF) approach which can be interpreted as a regularization of the Griffith's approach to brittle fracture following an energetic representation. Restricting the scope of the current study to the infinistesimal 2D deformation setting, we consider an arbitrary body in the general n_{dim} Euclidean space, denoted by $\mathcal{B} \in \mathbb{R}^{n_{dim}}$, with its external boundary $\partial\mathcal{B} \in \mathbb{R}^{n_{dim}-1}$, see Fig. 1. The displacement field at any material point $\mathbf{x} \in \mathcal{B}$ is identified by the vector $\mathbf{u} : \mathcal{B} \to \mathbb{R}^{n_{dim}}$, with infinitesimal strain tensor $\boldsymbol{\varepsilon} := \nabla^s \mathbf{u}$ for $\boldsymbol{\varepsilon} : \mathcal{B} \to \mathbb{R}^{n_{dim} \times n_{dim}}$. Prescribed boundary conditions are identified by $\mathbf{u} = \overline{\mathbf{u}}$ on $\partial\mathcal{B}_u$ and $\overline{\mathbf{t}} = \boldsymbol{\sigma} \cdot \mathbf{n}$ on $\partial\mathcal{B}_t$, satisfying $\partial\mathcal{B}_t \cup \partial\mathcal{B}_u = \partial\mathcal{B}$ and $\partial\mathcal{B}_t \cap \partial\mathcal{B}_u = \emptyset$, where $\mathbf{n}$ is outward normal vector and $\boldsymbol{\sigma}$ is the Cauchy stress tensor.

For arbitrary cracked bodies, the central idea of the PF method concerns the definition of a crack-like phase field variable $\mathfrak{d} : \mathcal{B} \times [0, t] \to [0, 1]$, permitting the identification of unbroken $\mathfrak{d}(\mathbf{x}, t) = 0$ and fully broken $\mathfrak{d}(\mathbf{x}, t) = 1$ states at $\mathbf{x} \in \mathcal{B}$, see Fig. 1. Therefore, for a given crack surface topology at time t as $\Gamma_c(t) \subset \mathbb{R}^{n_{dim}-1}$ in $\mathcal{B}$, the regularized crack functional is given by

$$\Gamma_c(\mathfrak{d}, t) := \int_{\mathcal{B}} \gamma(\mathfrak{d}, \nabla_{\mathbf{x}} \mathfrak{d}) \, \mathrm{d}\Omega, \tag{1}$$

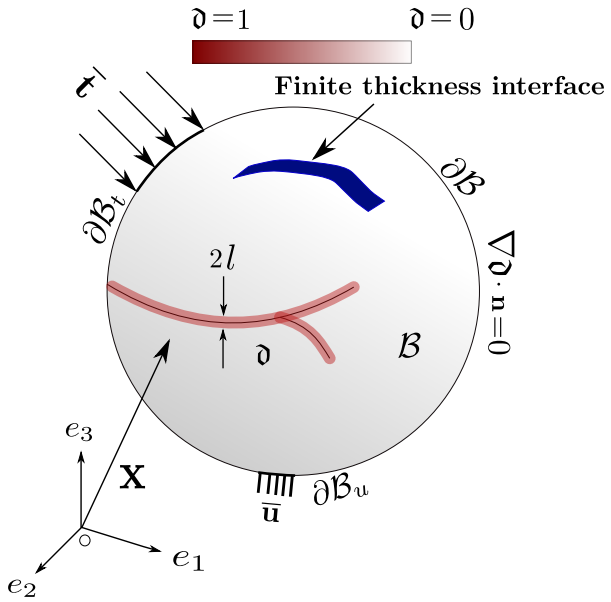

Figure 1: Schematic representation of the phase field representation of a cracked system with prescribed finite thickness interfaces.

where the so-called crack density functional in line with [21] is defined as:

$$\gamma(\mathfrak{d}, \nabla_{\mathbf{x}}\mathfrak{d}) := \frac{1}{2l}\mathfrak{d}^2 + \frac{l}{2}\left|\nabla_{\mathbf{x}}\mathfrak{d}\right|^2. \tag{2}$$

The irreversibility of the fracture process within the solid under consideration is dictated by the condition proposed in [21], such $\Gamma_c(\mathfrak{d}, t) \in \Gamma_c(\mathfrak{d}, t + \Delta t)$.

The minimization problem associated with the diffusive crack topology reads

$$\mathfrak{d}(\mathbf{x}, t) = \text{Arg}\{\inf_{\mathfrak{d}\in\mathcal{W}_{\Gamma(t)}} \Gamma_c(\mathfrak{d}, t)\} \tag{3}$$

under the Dirichlet-type constraint: $\mathcal{W}_{\Gamma(t)} = \{\mathfrak{d} \,|\, \mathfrak{d}(\mathbf{x}, t) = 1 \text{ at } \mathbf{x} \in \Gamma_c(\mathfrak{d}, t)\}$.

Consequently, the internal potential energy of the cracked body can be expressed as:

$$\Pi(\mathbf{u}, \Gamma) = \Pi_\Omega(\mathbf{u}, \Gamma) + \Pi_{\Gamma_c}(\Gamma) = \int_{\Omega\setminus\Gamma} \psi^e(\boldsymbol{\varepsilon})\, \mathrm{d}\Omega, + \int_{\Gamma_c} \mathcal{G}_c\, \mathrm{d}\Gamma, \tag{4}$$

where $\psi^e(\boldsymbol{\varepsilon})$ stands for the elastic energy density and $\mathcal{G}_c$ corresponds to the fracture toughness. Moreover, note that in the previous expression, two contri-

butions can be recalled: $\Pi_\Omega(\mathbf{u},\Gamma)$ is the elastic energy stored in the damaged body, while $\Pi_\Gamma(\Gamma)$ is the dissipative term complying with the Griffith's approach to fracture.

By the virtue of Γ-convergence concept [22], the fracture term can be approximated as:

$$\int_{\Gamma_c} \mathcal{G}_c \, \mathrm{d}\Gamma \approx \int_{\mathcal{B}} \mathcal{G}_c \gamma(\mathfrak{d}, \nabla_{\mathbf{X}} \mathfrak{d}) \, \mathrm{d}\Omega. \tag{5}$$

In the presence of prescribed thin interfaces within the systems domain, Paggi and Reinoso [18] proposed an original modelling framework comprising the combined use of PF and cohesive-like cracking models for bulk and interface fracture events, respectively. This differentiation between dissipative phenomena from different signature can be introduced via the adoption of the following split:

$$\Pi_{\Gamma_c} = \Pi_{\Gamma_b} + \Pi_{\Gamma_i} = \int_{\Gamma_b} \mathcal{G}_c^b(\mathbf{u},\mathfrak{d}) \, \mathrm{d}\Gamma + \int_{\Gamma_i} \mathcal{G}^i(\mathbf{u},\mathfrak{d}) \, \mathrm{d}\Gamma, \tag{6}$$

where $\mathcal{G}_c^b$ is the bulk fracture energy and $\mathcal{G}^i$ is the energy dissipated along the prescribed interfaces of the system. This latter contribution can be expressed in terms of displacement discontinuities along the interface, $\mathbf{g}$, the interface history parameter, $\mathfrak{h}$, and the phase field degradation variable of the surrounding bulk $\mathfrak{d}$:

$$\mathcal{G}^i = \mathcal{G}(\mathbf{g}, \mathfrak{h}, \mathfrak{d}). \tag{7}$$

The previous decomposition leads to the form of the internal potential of the system (composed by the bulk $\Pi_b(\mathbf{u},\mathfrak{d})$ and the interface contributions $\Pi_i(\mathbf{u},\mathfrak{d})$):

$$\Pi_b(\mathbf{u},\mathfrak{d}) = \int_\Omega \underbrace{\psi(\boldsymbol{\varepsilon},\mathfrak{d})}_{\psi_e^b} \, \mathrm{d}\Omega + \int_\Omega \underbrace{\mathcal{G}_c^b \gamma(\mathfrak{d}, \nabla_{\mathbf{x}} \mathfrak{d})}_{\psi_{fr}^b} \, \mathrm{d}\Omega, \tag{8}$$

$$\Pi_i(\mathbf{u},\mathfrak{d}) = \int_{\Gamma_i} \underbrace{\mathcal{G}^i(\mathbf{u},\mathfrak{d})}_{\psi_{fr}^i} \, \mathrm{d}\Gamma, \tag{9}$$

where $\psi(\boldsymbol{\varepsilon}, \mathfrak{d})$ is the energy density of the bulk for the damaged state, whose positive part is affected by the degradation function: $\mathfrak{g}(\mathfrak{d}) = (1-\mathfrak{d})^2 + \mathcal{K}$, being $\mathcal{K}$ a parameter that defines a residual stiffness to prevent numerical instabilities. Note that we adopt the spectral decomposition of the elastic energy advocated in [21]:

$$\psi(\boldsymbol{\varepsilon}, \mathfrak{d}) = \mathfrak{g}(\mathfrak{d})\psi_+^e(\boldsymbol{\varepsilon}) + \psi_-^e(\boldsymbol{\varepsilon}), \tag{10a}$$

$$\psi_+^e(\boldsymbol{\varepsilon}) = \frac{\lambda}{2}\left(\langle \mathrm{tr}[\boldsymbol{\varepsilon}]\rangle_+\right)^2 + \mu \mathrm{tr}[\boldsymbol{\varepsilon}_+^2], \tag{10b}$$

$$\psi_-^e(\boldsymbol{\varepsilon}) = \frac{\lambda}{2}\left(\langle \mathrm{tr}[\boldsymbol{\varepsilon}]\rangle_-\right)^2 + \mu \mathrm{tr}[\boldsymbol{\varepsilon}_-^2]. \tag{10c}$$

The irreversibility aforementioned can be expressed in terms of the phase field variable using a local history field of the crack driving force [21]:

$$\mathcal{H}(\mathbf{x}, t) = \max_{\tau \in [0,t]} \psi_+^e(\boldsymbol{\varepsilon})(\mathbf{x}, t), \tag{11}$$

where $\mathcal{H}(\mathbf{x}, t)$ stands for the maximal value of the positive part of the elastic energy $\psi_+^e(\boldsymbol{\varepsilon})$.

Following [18, 10] and for the sake of simplicity, we herewith assume that the interface response is ruled by a simple tension cut-off cohesive zone model, where a linear variation of the critical normal, $g_{nc}(\mathfrak{d})$, and tangential, $g_{tc}(\mathfrak{d})$, relative displacements at the internal discontinuities (interface) can be stated in terms of the crack phase field variable of the bulk:

$$g_{nc}(\mathfrak{d}) \quad = (1-\mathfrak{d})g_{nc,0} + \mathfrak{d} g_{nc,1} \tag{12}$$

$$g_{tc}(\mathfrak{d}) \quad = (1-\mathfrak{d})g_{tc,0} + \mathfrak{d} g_{tc,1} \tag{13}$$

with $g_{nc,0} = g_{nc}(\mathfrak{d}=0)$ $g_{nc,1} = g_{nc}(\mathfrak{d}=1)$; and $g_{tc,0} = g_{tc}(\mathfrak{d}=0)$ and $g_{tc,1} = g_{tc}(\mathfrak{d}=1)$. A graphical representation of the Mode I and Mode II cohesive laws is provided in Fig. 2.

The cohesive traction for fracture Mode I, according to the tension cut-off

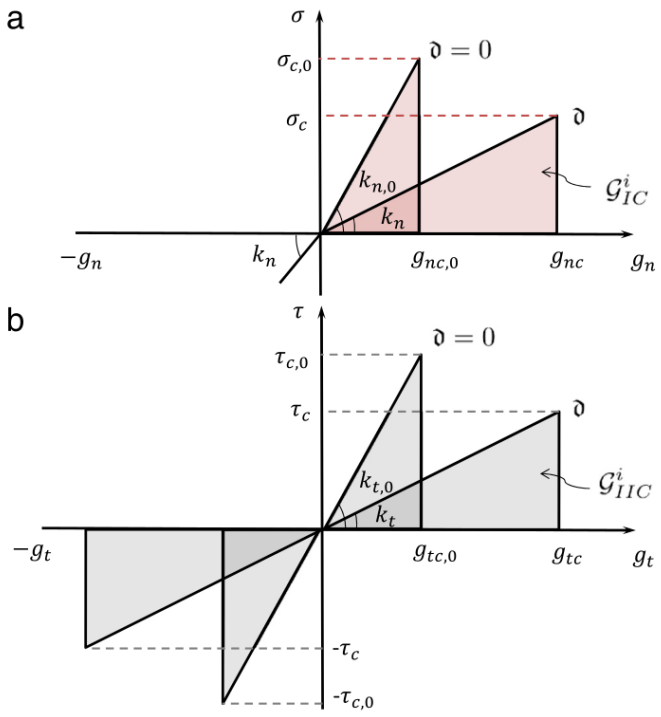

Figure 2: Schematic representation of the cohesive zone model coupled with the phase field variable for brittle fracture in the bulk: (a) Mode I CZM; (b) Mode II CZM.

model, is given by

$$\sigma = \begin{cases} k_n \dfrac{g_n}{g_{nc}}, & \text{if } 0 < \dfrac{g_n}{g_{nc}} < 1; \\ 0, & \text{if } \dfrac{g_n}{g_{nc}} \geq 1, \end{cases} \tag{14}$$

where σ is the normal traction component of the interface, being σ_c its corresponding critical value. This leads to the computation of the Mode I interface fracture energy:

$$\mathcal{G}^i_{Ic} = \frac{1}{2} k_n g^2_{nc}. \tag{15}$$

Imposing the condition that $\mathcal{G}^i_{Ic}$ is constant with respect to the phase field variable $\mathfrak{d}$, the apparent interface stiffness k_n takes the form:

$$k_n = k_{n,0} \left(\frac{g_{nc,0}}{g_{nc}} \right)^2, \tag{16}$$

where $k_{n,0}$ is the interface stiffness for $\mathfrak{d} = 0$. Moreover, due to the above constraint, the Mode I energy release rate, whose functional dependence is expressed in Eq. (7), takes the following closed-form expression:

$$\mathcal{G}_I^i = \frac{1}{2} k_{n,0} g_n^2 \frac{g_{nc,0}^2}{\left[(1-\mathfrak{d})\, g_{nc,0} + \mathfrak{d} g_{nc,1}\right]^2}, \tag{17}$$

The same constitutive hypothesis is assumed for the interface response under the fracture Mode II, leading to the following definition of the corresponding traction τ (whose critical value is identified by τ_c):

$$\tau = \begin{cases} k_t \dfrac{g_t}{g_{tc}}, & \text{if } 0 < \dfrac{g_t}{g_{tc}} < 1; \\ 0, & \text{if } \dfrac{g_t}{g_{tc}} \geq 1. \end{cases} \tag{18}$$

Thus, the apparent stiffness for the fracture Mode II, k_t, renders:

$$k_t = k_{t,0} \left(\frac{g_{tc,0}}{g_{tc}} \right)^2. \tag{19}$$

With the above definitions, the Mode II interface fracture energy is given by

$$\mathcal{G}_{IIc}^i = \frac{1}{2} k_t g_{tc}^2. \tag{20}$$

Hence, the Mode II energy release rate reads:

$$\mathcal{G}_I^i = \frac{1}{2} k_{n,0} g_n^2 \frac{g_{nc,0}^2}{\left[(1-\mathfrak{d})\, g_{nc,0} + \mathfrak{d} g_{nc,1}\right]^2}, \tag{21}$$

Finally, a standard quadratic criterion is used to govern the interface fracture under Mixed Mode conditions:

$$\left(\frac{\mathcal{G}_I^i}{\mathcal{G}_{Ic}^i} \right)^2 + \left(\frac{\mathcal{G}_{II}^i}{\mathcal{G}_{IIc}^i} \right)^2 = 1, \tag{22}$$

where:

$$\mathcal{G}_{Ic}^i = \frac{1}{2} g_{nc,0}^2 k_{n,0}; \quad \mathcal{G}_{IIc}^i = \frac{1}{2} g_{tc,0}^2 k_{t,0}. \tag{23}$$

2.2. Extension for dynamic fracture of the combined PF-CZM modeling framework

The central development of the current investigation concerns with the extension of the modelling framework presented above for triggering dynamic fracture events in heterogeneous media with the presence of thick interfaces.

Recalling [12, 13, 14], the kinetic energy of the system (including the bulk and interface terms) can be expressed as:

$$K = \int_{\mathcal{B}} \psi^b_{kin} \, \mathrm{d}\Omega + \int_{\Gamma_i} \psi^i_{kin} \, \mathrm{d}\Gamma, \tag{24}$$

$$\psi^b_{kin} = \frac{1}{2}\rho_b \dot{\mathbf{u}} \cdot \dot{\mathbf{u}} \quad \psi^i_{kin} = \frac{1}{2}\rho_i h \dot{\mathbf{u}} \cdot \dot{\mathbf{u}} \tag{25}$$

where ρ_b is the density of the bulk, ρ_i is the density of the finite interface and h is the interface thickness.

Accordingly, it is possible to compute the Lagrangian L of the system:

$$\begin{aligned} L = K - \Pi \quad &= \textstyle\int_{\mathcal{B}} \mathcal{L}^b(\mathbf{u}, \dot{\mathbf{u}}, \mathfrak{d}, \nabla_{\mathbf{x}} \mathfrak{d}) \, \mathrm{d}\Omega + \\ &\textstyle\int_{\Gamma_i} \mathcal{L}^i(\mathbf{u}, \dot{\mathbf{u}}, \mathfrak{d}) \, \mathrm{d}\Gamma + \Pi_{ext}, \end{aligned} \tag{26}$$

with Π_{ext} denoting the exterior potential due to the prescribed loadings, and

$$\mathcal{L}^b(\mathbf{u}, \dot{\mathbf{u}}, \mathfrak{d}, \nabla_{\mathbf{x}} \mathfrak{d}) = \psi^b_{kin} - \psi^b_e - \psi^b_{fr} \tag{27}$$

$$\mathcal{L}^i(\mathbf{u}, \dot{\mathbf{u}}, \mathfrak{d}) = \psi^i_{kin} - \psi^i_{fr}. \tag{28}$$

The terms defined in Eqs.(27)–(28) denote the Lagrange density per unit of volume and surface corresponding to the bulk and the interfaces, respectively.

The Hamilton's principle is given by

$$\int_{t_1}^{t_2} \left[\int_{\mathcal{B}} \delta\mathcal{L}^b \, \mathrm{d}\Omega + \int_{\Gamma_i} \delta\mathcal{L}^i \, \mathrm{d}\Gamma + \delta\Pi_{ext}, \right] \mathrm{d}t = 0, \tag{29}$$

for arbitrary times $t_1 < t_2$. The corresponding variations of the Lagrange densities can be expressed as:

$$\begin{aligned} \delta\mathcal{L}^b \quad &= \tfrac{\partial \mathcal{L}^b}{\partial \mathbf{u}} \cdot \delta\mathbf{u} + \tfrac{\partial \mathcal{L}^b}{\partial \dot{\mathbf{u}}} \cdot \delta\dot{\mathbf{u}} + \tfrac{\partial \mathcal{L}^b}{\partial \nabla_{\mathbf{x}} \mathbf{u}} : \nabla_{\mathbf{x}} \delta\mathbf{u} + \\ &\tfrac{\partial \mathcal{L}^b}{\partial \mathfrak{d}} \delta\mathfrak{d} + \tfrac{\partial \mathcal{L}^b}{\partial \nabla_{\mathbf{x}} \delta\mathfrak{d}} \cdot \nabla_{\mathbf{x}} \delta\mathfrak{d} \end{aligned} \tag{30}$$

$$\delta\mathcal{L}^i = \frac{\partial \mathcal{L}^i}{\partial \mathbf{u}} \cdot \delta\mathbf{u} + \frac{\partial \mathcal{L}^i}{\partial \dot{\mathbf{u}}} \cdot \delta\dot{\mathbf{u}} + \frac{\partial \mathcal{L}^i}{\partial \mathfrak{d}} \delta\mathfrak{d}. \tag{31}$$

After some algebraic manipulations, the Euler-Lagrange equations of the variational principle leads to the equations of motions

$$\rho\ddot{\mathbf{u}} - \nabla_{\mathbf{x}} \cdot \boldsymbol{\sigma} = \mathbf{0}, \tag{32}$$

and the crack phase field evolution

$$2(1-\mathfrak{d})\psi_+^e(\boldsymbol{\varepsilon}) = \mathcal{G}_c^b \left[\frac{1}{l} + l\nabla_{\mathbf{x}}\mathfrak{d}\right] + \frac{\partial \mathcal{G}^i}{\partial \mathfrak{d}}. \tag{33}$$

Note that Eqs. (32)–(33) govern the dynamic diffusive crack propagation problem in systems with the presence of prescribed finite thickness interfaces.

Through the exploitation of the previous formulation, it is possible the construction of the corresponding numerical formulation within the spirit of multi-field whereby the displacements and the crack phase field variable are the primary unknowns $\{\mathbf{u}, \mathfrak{d}\}$. Within the context of the Finite Element Method (FEM), we advocated a Jacobi-type staggered solution scheme in line with the numerical implementation into the FE code FEAP [23] using a Newmark-type constant-average-acceleration scheme. Details of the bulk phase field model and the dynamic interface formulation can be respectively found in [12, 19], which are omitted here for the sake of brevity.

3. Representative applications

In this section, we demonstrate the numerical capability of the current dynamic PF-CZM formulation for triggering fracture events in heterogeneous media in dynamics. The application under study consists of a primary crack perpendicular to an interface (separating two solids), Fig. 3. This specimen is made from PMMA, whose mechanical properties are listed in Table 1.

The geometry of the specimen is a rectangular domain with dimensions 40×43 (lengths in mm), and with an edge crack of 6 mm in length. The vertical

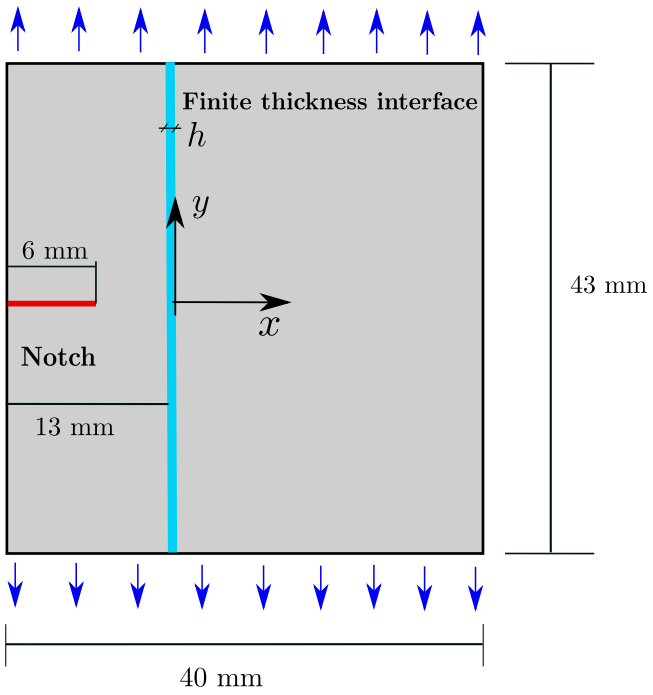

Figure 3: Specimen description and loading conditions.

interface is defined at 13 mm from the left side of the plate. The thickness is unitary. This system is subjected to a displacement rate applied to the top and bottom sides, according to the scheme depicted in Fig. 3. The displacement rate starts from zero and increases, following a specific ramp function designed to minimize the effect of spurious vibrations, up to a steady-state value, corresponding to a strain rate of $\dot{\varepsilon}_y = 100$ s^{-1}. The length of the ramp is 31μs, while the crack initiation, as it will be discussed later, occurs at about 73μs. Therefore, the crack propagation takes place in the steady-state regime and it is not influenced by the loading ramp. More details about the definition of the loading ramp can be found in ref. [20] Regarding the FE discretization, the system is meshed using 4-node quadrilateral elements with size equal to 0.2 mm, and an increment time step in the solution scheme corresponding to 1 μs. The value of the phase field regularization length, parameter l in Eq. (2), has been set equal to 30μm. Such a parameter has been tuned through preliminary

numerical simulations on un-notched specimens, in order to retrieve the correct material average strength, equal to 55 MPa for PMMA.

E_b [GPa]	ν	$\mathcal{G}_c^b$ [J/m^2]	σ_c^b [MPa]	ρ_b [kg/m^3]
3	0.35	300	55	1180

Table 1: Material properties of PMMA.

With respect to the interface, we consider two possible configurations depending on the thickness: (*i*) a thin interface, 0.2 mm thick, and (*ii*) a thick interface, 1.0 mm thick. Moreover, we adopt the following assumptions:

- The apparent stiffness of the cohesive law (both Mode I and Mode II) is given by the ratio between the Young's modulus of the material constituting the interface and the interface thickness, $k_{n,t} = E_i/h$.
- The interface mass increases with its thickness, since the interface density is multiplied by the thickness value in the corresponding formulation.
- The critical stress of the interface σ_c^i, i.e., the peak stress of the cohesive law, decreases with the thickness, whereas the fracture energy is kept constant.

The latter hypothesis is supported by the results of several experiments and the prediction of analytical models available in the literature, especially for adhesives having a hyperelastic behaviour [24, 25, 26]. Moreover, it is also an obvious choice, consequent to the use of the tension cut-off cohesive law. In fact, only two out of the four parameters, namely initial stiffness, peak stress, fracture energy and critical relative displacement, are independent. The other two parameters are determined through Eqs.(14) and (15) for Mode I and Eqs.(18) and (20) for Mode II.

No specific material has been defined for the interface. However, the reference material properties are representative of a generic polymeric resin: E_i = 0.7 GPa and $\mathcal{G}_c^i = 410$ J/m^2. The full set of parameters for the two interfaces

are given in Table 2. Note also that in this study, for the sake of simplicity, we set identical mechanical properties for fracture Modes I and II of the interface and no coupling between the critical gap of the interface for intact and fully damaged states of the surrounding bulk.

h [mm]	$k_{n,t}$ [N/mm^3]	$\mathcal{G}_c^i$ [J/m^2]	σ_c^i [MPa]	g_c [μm]	ρ_i [kg/m^3]
0.2	3500	410	53.6	15.2	1200
1	700	410	24.0	34.2	1200

Table 2: Material properties of the interface: thin and thick scenarios.

As discussed in [18], the total force carried by the specimen can be considered as the representative system response, which can be accounted for via the functional:

$$F = F\left(\sigma_c^i, \mathcal{G}_c^b, \mathcal{G}_c^i, E_i, \nu, l, L, \Delta\right). \tag{34}$$

where l is the regularization length of the phase field formulation, L is the characteristic sample size, and Δ is the imposed displacement at the sample's boundaries. Through the invocation of the Π-theorem of dimensional analysis, the following dimensionless representation is derived by selecting σ_c^i and L as the physical independent quantities:

$$\frac{F}{\sigma_c^i L^2} = \Phi\left(\frac{\mathcal{G}_c^b}{\mathcal{G}_c^i}, \frac{\mathcal{G}_c^i E_i}{\left(\sigma_c^i\right)^2 L}, \nu, \frac{l}{L}, \frac{\Delta}{L}\right) = \Phi\left(\Pi_1, \Pi_2, \nu, \frac{l}{L}, \frac{\Delta}{L}\right) \tag{35}$$

where it is possible to recognize that the second dimensionless number Π_2 is proportional to the ratio between the process zone size along the interface, $l_{\mathrm{CZM}} \sim \left(\mathcal{G}_c^i E_i\right)/(\sigma_c^i)^2$, and the characteristic sample size, L. Therefore, the use of Linear Elastic Fracture Mechanics (LEFM) results is retrieved in the limit case $\Pi_2 \to 0$. This analysis is herewith exploited in order to shed light to the differences between static and dynamic fracture propagation.

3.1. Thin interface case: numerical predictions

This section presents the analysis of the thin interface case. Exploiting the dimensional analysis presented above, this scenario can be examined with LEFM

results under quasi-static conditions, leading to $\Pi_1 = 0.73$ and $\Pi_2 = 0.0025$ and predicting crack penetration into the secondary body with no interface failure. This result is in good agreement with the current numerical prediction as shown by the crack pattern in Fig. 4. The absence of interface delamination is confirmed by the evolution of the tangential gap along the interface in the range $y = [0, 21.5]$ mm, shown in Fig. 5a for three significant steps of crack propagation: initiation (step no. 75), interface crossing (step no. 100), and complete propagation (step no. 130). Here, the tangential gap remains close to zero and, in any case, much lower than the critical value corresponding to complete delamination, $g_{tc} = 15.3\mu$m. For dynamic fracture, the corresponding prediction exhibits appreciable differences with respect to the quasi-static case. Under such configuration, the proposed modelling approach estimates a crack propagation into the first bulk till the crack impinges onto the finite thickness interface, which is followed by the occurrence of very moderate delamination events, see the evolution of the tangential gap along the interface for different time steps in Fig. 5b. Subsequently, the crack further propagates through the second bulk following a straight path.

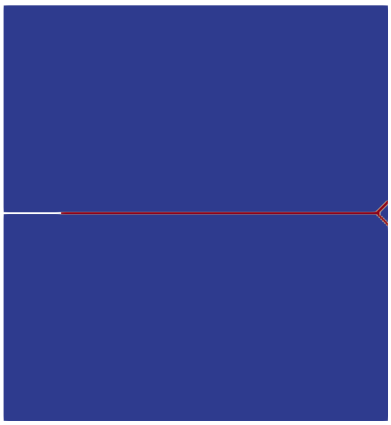

Figure 4: Crack path for the quasi-static loading condition, thin interface configuration.

The evolution of the crack path is shown in Fig. 6 with the indication of the time step of significant events. The crack starts to propagate at $t = 73\mu$s,

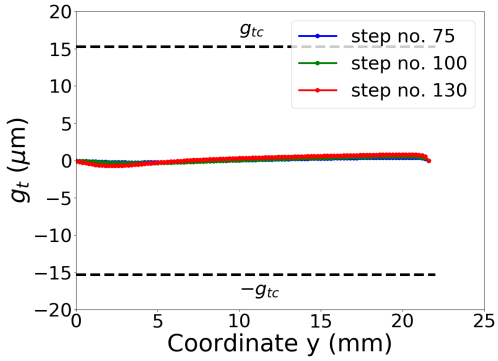

(a)

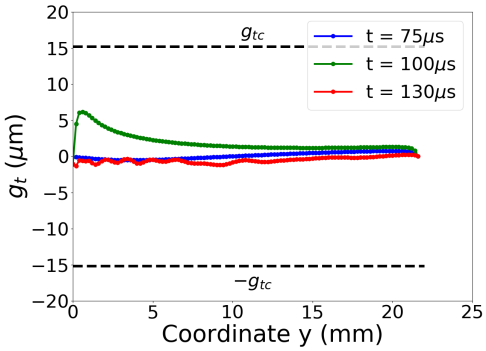

(b)

Figure 5: Evolution of the tangential gap along the thin interface for different simulation steps: (a) quasi-static loading condition; (b) dynamic loading condition.

impinges on the interface at $t = 99\mu$s, and penetrates in the second bulk at $t = 100\mu$s. Therefore, there is no time delay when the crack meets the interface. The average crack propagation speed is about 440 m/s, far below the limiting velocity $0.7c_R$ above which crack branching takes place [27, 16]. Note that c_R is the Rayleigh wave speed, equal to about 900 m/s for PMMA. This confirms that crack branching cannot occur. The stress-displacement curves for the quasi-static and dynamic cases are shown in Fig. 7. The stress is the average value computed with reference to the size of the initial ligament of the specimen, i.e. 34 mm, while the displacement is the total elongation of the specimen in the loading direction. Compared to the quasi-static case, the dynamic response is

characterised by a higher peak load due to inertia effects and a larger energy dissipation due to a thickening of the damaged zone, which is usually interpreted as representative of the appearance of micro-branches.

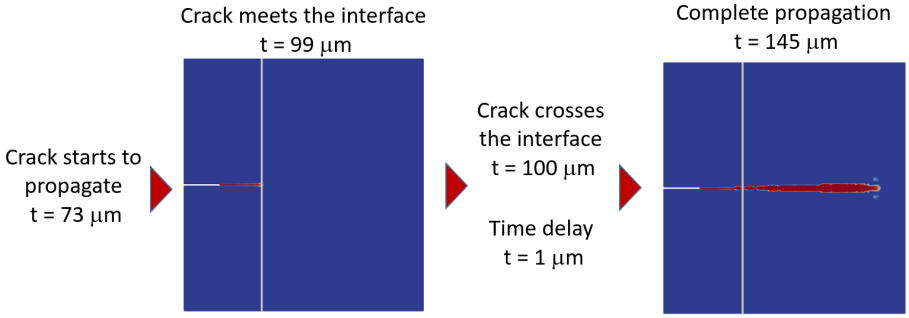

Figure 6: Evolution of the crack path and time elapsed during the crack propagation for the thin interface configuration in dynamic loading conditions.

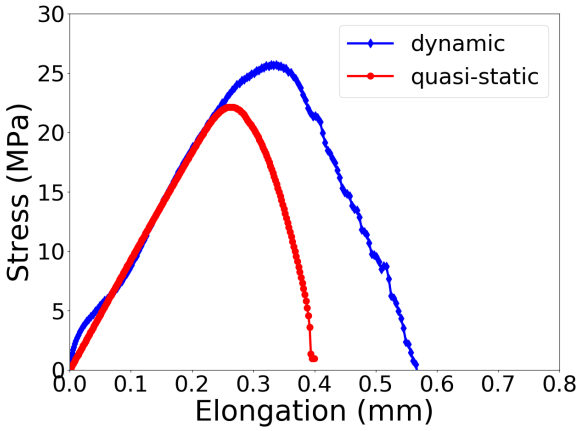

Figure 7: Stress - elongation curves for thin interface, quasi-static and dynamic loading conditions.

3.2. Thick interface case: numerical predictions

This section comprises the analysis of the interface 1 mm thick. In line with the previous results, the dimensional analysis under quasi-static conditions allows computing $\Pi_1 = 0.73$ and $\Pi_2 = 0.012$ and again predicting crack

penetration into the secondary body with absence of delamination events. Such a prediction finds again confirmation in the results of the numerical simulations, being the crack path identical to that obtained in the case of thin interface (see Fig. 4), and the evolution of the tangential gap along the interface that shown in Fig. 8a. The tangential gaps are slightly larger than the thin interface case, although their values remain much lower than the critical value g_{tc}. Note that, due to different material properties, g_{tc} for the thick interface is equal to 34.2μm.

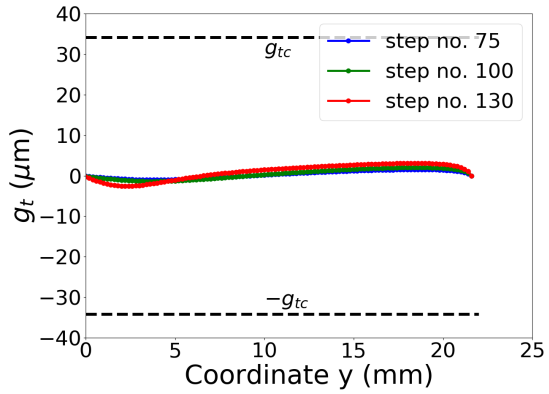

(a)

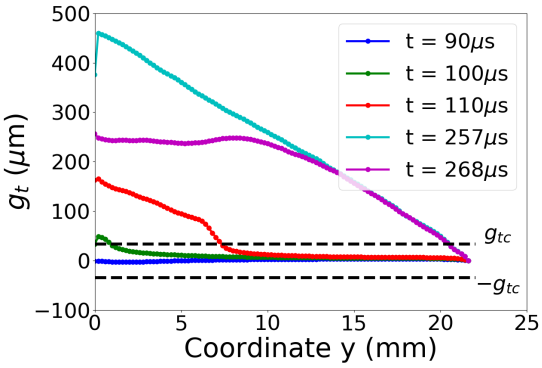

(b)

Figure 8: Evolution of the tangential gap along the thick interface for different simulation steps: (a) quasi-static loading condition; (b) dynamic loading condition.

However, in contrast to the precedent case, the current scenario presents significant differences between the quasi-static and the dynamic case, as high-

lighted in the sequence of the crack propagation shown in Fig. 9. The crack initiates propagating at $t = 73\mu$s, reaches the interface at $t = 99\mu$s, and penetrates in the second bulk at $t = 256\mu$s. Therefore, a significant time delay of $\Delta t = 157\mu$s is accumulated when the crack meets the interface before penetrating in the second layer. In order to better understand the origin of such a delay, the evolution of the tangential gap (sliding displacement of layer two with respect to layer one) along the common interface for different time steps is analyzed in Fig. 8b. The tangential gap is almost zero until the crack reaches the interface. Then, it gradually increases, from the center to the edge of the specimen, and rapidly overcomes the value of g_{tc}, up to a complete delamination along most of the interface length. The tangential gap increases monotonically up to $t = 257\mu$s, i.e. the instant of crack penetration into the second bulk. Then, a partial elastic recovery is obtained. Besides the time delay in the crack propagation, the interplay between crack propagation in the bulk and interface delamination described above leads to a dynamic crack branching in the second bulk. The origin for such a behaviour lies in the fact that during the interface delamination energy continues to be accumulated up to the point where the crack initiates penetrating into the second layer. Hence, the crack enters the second bulk with a high acceleration and it branches as soon as its velocity approaches the limiting speed of $0.7c_R$.

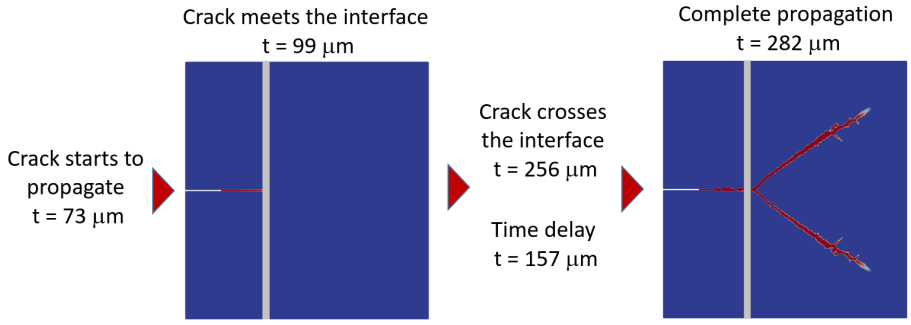

Figure 9: Evolution of the crack path and time elapsed during the delamination events at the thick interface.

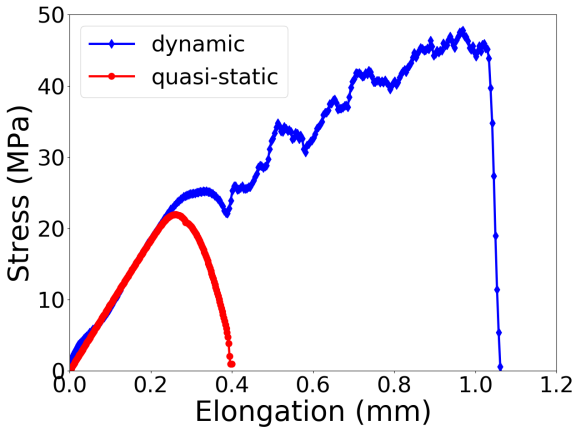

Figure 10: Stress - elongation curves for thick interface, quasi-static and dynamic loading conditions.

Significant differences are also obtained on the stress-displacement behaviour. The curves related to the quasi-static and dynamic cases with a thick interface are shown in Fig. 10. The quasi-static behaviour is coincident with that of the thin interface shown in Fig. 7. On the contrary, the dynamic behaviour is very different. Quasi-static and dynamic curves are coincident up to the first peak, when interface delamination initiates in the dynamic case. Then, a hardening branch occurs in dynamic loading conditions, whereas a softening post-peak behaviour is obtained in quasi-static loading. Crack penetrates in the second bulk at the end of the hardening phase. The maximum load in dynamics is about twice the peak load measured in the quasi-static case. Such a large increase is due to the fact that the interface acts as a shield against crack propagation. In case of a thick interface, in fact, the second bulk is only slightly affected by the stress concentration ahead of the crack tip.

The obtained numerical predictions are in qualitatively agreement with the results of experimental tests available in the literature such as, for instance, those carried out by Xu and Rosakis [28] and by Parab and Chen [29]. Xu and Rosakis studied the dynamic failure in two- and three-layer bonded Homalite specimens featuring different bonding strengths. The crack patterns obtained for an impact

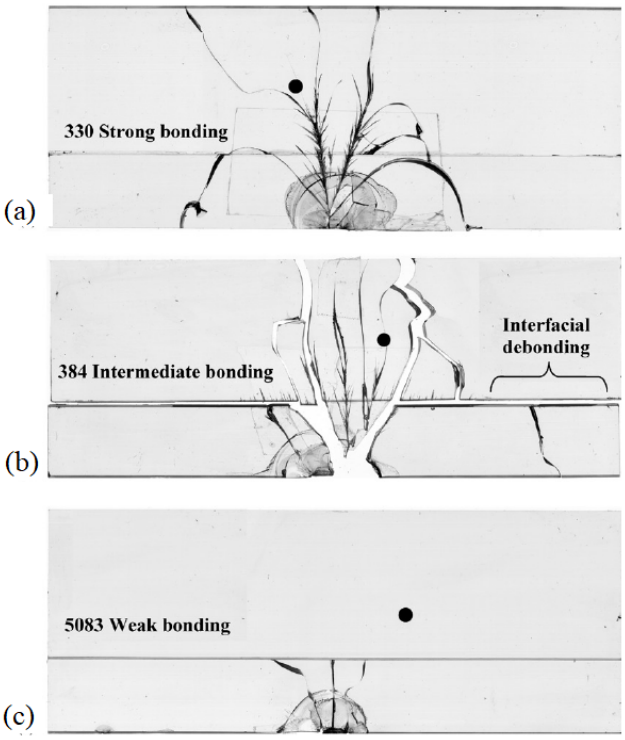

Figure 11: Experimental evidences of the effect of the interface strength on the dynamic crack propagation through layered materials (adapted from [28]).

speed of 21 m/s, shown in Fig. 11, are highly dependent on the bonding strength, with the appearance of interfacial debonding in case of intermediate and weak bonding that shield, partially or totally, the second layer from crack penetration. Parab and Chen studied the dynamic crack propagation across an adhesive interface in borosilicate glass. Three different interface thicknesses were studied, namely $h = 0.2$, 1.0 and 2.7 mm. The crack patterns obtained for $h = 0.2$ and 1.0 mm are shown in Fig. 12. Two main differences were observed by increasing the interface thickness: the occurrence of crack branching in the second plate and an increase of the delay in the crack propagation across the interface (8.2μs for $h = 0.2$ mm compared to 60.4μs for $h = 1.0$ mm).

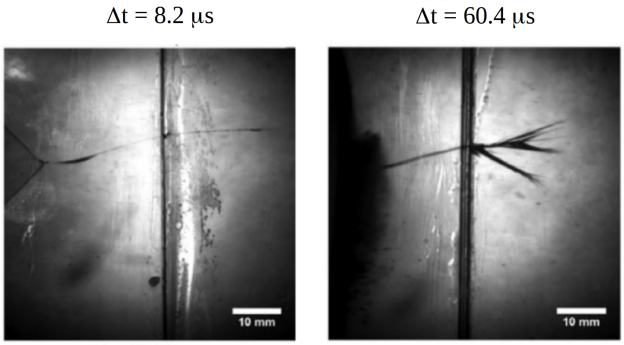

(a) Interface thickness 0.2 mm (b) Interface thickness 1.0 mm

Figure 12: Experimental evidences of the effect of the interface thickness on the dynamic crack propagation through layered materials (adapted from [29]).

4. Parametric study

A parametric study has been carried out to analyse the effect of the properties of the interface on the dynamic failure of layered materials, with special regard to the competition between interface debonding, crack penetration and branching. A total of eleven different cohesive constitutive laws were considered: five for the thick interface, $h = 1.0$ mm, and six for the thin interface, $h = 0.2$ mm. The set of material properties are reported in Table 3, while a simplified graphical representation of the corresponding pure Mode II is shown in Fig. 13. The reference case for $h = 1.0$ mm is Case 1, which has the same properties of the constitutive law adopted in the previous section for the same interface. In Cases 2 and 3 the interface stiffness was changed to 3000 and 140 $\mathrm{N/mm^3}$, respectively, while the fracture energy was kept constant. In Cases 4 and 5 the fracture energy was changed to 820 and 205 J/m, respectively, while the interface stiffness was kept constant. In all the cases, the other two parameters, namely critical stress and critical gap, have been computed through Eqs. 14 and 15 for Mode I and Eqs. 18 and 19 for Mode II. Starting from Case 6, which is the reference case for the interface 0.2 mm thick, the interface stiffness was varied in Cases 7 and 8, whereas the fracture energy was varied in Cases 9, 10 and 11. Again, the critical stress and the critical gap were computed

accordingly.

Id. code	h [mm]	$k_{n,t}$ [N/mm^3]	$\mathcal{G}_c^i$ [J/m^2]	σ_c^i [MPa]	g_c [μm]
1	1.0	700	410	24.0	34.2
2	1.0	3000	410	49.6	16.5
3	1.0	140	410	10.8	75.9
4	1.0	700	820	33.9	48.4
5	1.0	700	205	16.9	24.3
6	0.2	3500	410	53.6	15.3
7	0.2	15000	410	110.9	7.4
8	0.2	700	410	24.0	34.2
9	0.2	3500	820	75.8	21.6
10	0.2	3500	205	37.9	10.8
11	0.2	3500	102	26.8	7.6

Table 3: Set of material properties of the eleven interfaces considered in the parametric study.

The numerical simulations confirms the two main behaviours observed in Section 3: the dynamic propagation of a single crack through the two bodies without any delay in crossing the interface is predicted in Cases 2, 4, 6, 7, 9 and 10, whereas a delay in the crack propagation between the first and the second body and a crack branching are predicted in Cases 1, 3, 5, 8 and 11. All the cases characterised by a single straight crack present features for what concerns crack propagation timing, distribution of gaps along the interface and stress vs. elongation overall response very similar to the reference case, presented in Section 3. On the other hand, more interesting results were obtained with the cases characterised by time delay and crack branching. In particular, Cases 3 and 8 behaves as Case 1, whereas Cases 5 and 11 present the following differences with respect to Case 1: time delay in crossing the interface of 110μs instead of 157μs, crack branching at about 8 mm behind the interface instead of just after the interface, complete failure of the specimen after 250μs instead of 282μs, and peak stress in the stress vs. elongation diagram slightly lower than the reference

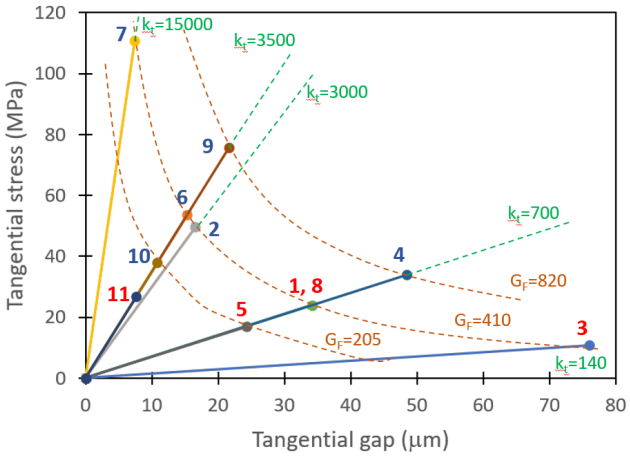

Figure 13: Representation of the eleven cohesive constitutive laws whose parameters are reported in Table 3. The values of the fracture energy and interface stiffness are also reported.

case. The shorter time delay in crossing the interface leads to a reduced amount of energy stored in the second bulk and, therefore, a translation of the branching point. The final crack patterns for Cases 5 and 11 are shown in Fig. 14, while the stress vs. elongation curves for all the specimens are depicted in Fig. 15. By analysing the constitutive laws shown in Fig. 13 it emerges that all the specimens exhibiting delay in the crack propagation and crack branching are characterised by an interface having a low value of critical stress, independently of the other parameters. However, also the critical gap and, therefore, the fracture energy, play a role in the dynamic fracture (see, for instance, specimens 5 and 11, which have low values of both critical stress and critical gap).

Finally, the effect of the loading rate was investigated with the two reference Cases 1 and 6, by increasing the strain rate to $\dot{\varepsilon}_y = 1000$ s^{-1}. In the specimen with the thick interface, crack initiates to propagate at $t = 50\mu$s, impinges on the interface at $t = 80\mu$s and penetrates in the second layer without any delay. It branches at $t = 84\mu$s. The high energy accumulated determines the appearance of a multiple branching just behind the interface (see Fig. 16a). The absence of time delay is consistent with the interface debonding, that is greatly reduced

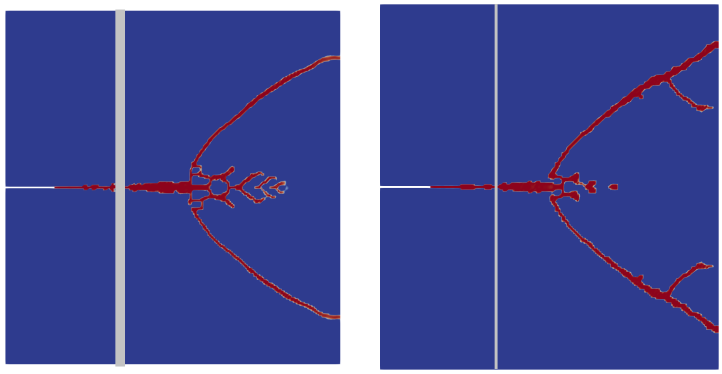

(a) (b)

Figure 14: Crack patterns obtained for: (a) Case 5 and (b) Case 11.

compared to the reference Case 1 (see Fig. 16b). When the crack penetrates in the second layer, only a little portion of interface is debonded. The behaviour of the specimen with the thin interface subjected to the strain rate $\dot{\varepsilon}_y = 1000$ s^{-1} is completely different from the reference Cases 1 and 6. In this case, two main crack branching events occur, one in the first layer, at $t = 74\mu$s, and another just behind the interface, at $t = 78\mu$s (see Fig. 17a). The diagrams of the tangential gaps along the interface at different time steps shown in Fig. 17b prove that the interface does not fail, since the gap is always below the critical value. No time delay has been observed. Concerning the obtained crack patterns, it is to be noticed that the increase in strain rate makes more evident the boundary effects, that manifest through the appearance of two cracks initiated at the right edge (see Figs. 16a and 17a).

5. Conclusions

In this study, a consistent extension to the dynamic regime of the PF model for triggering fracture events in heterogeneous media including finite thickness cohesive interfaces proposed in [18] has been carried out. The current formulation endowed a simple treatment of the presence of finite thickness interfaces through their consideration via a cohesive-like crack representation.

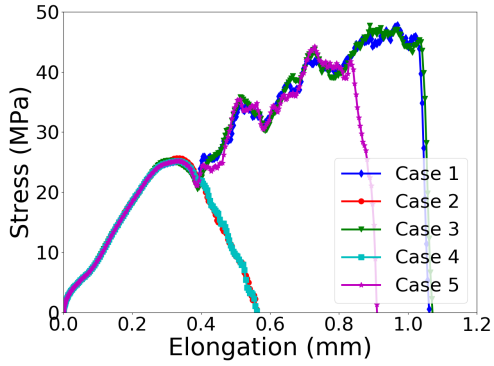

(a)

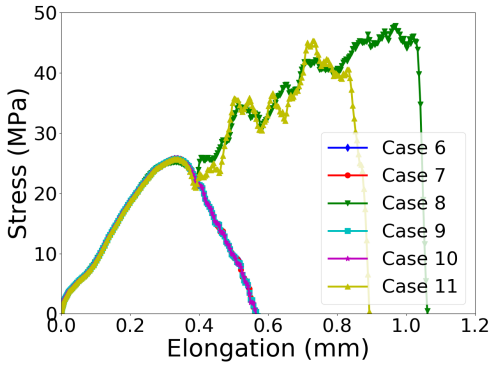

(b)

Figure 15: Stress-elongation curves for: (a) Cases 1 to 5 and (b) Cases 6 to 11.

Through the use of the present approach, we have analysed different scenarios of primary cracks impinging on interfaces with different thickness. Current results exhibited significant differences depending upon the interface thickness, stiffness and strength in terms of crack propagation delay and secondary branching into the adjoining bulk. These predictions were in good agreement with respect to available experimental data [28, 29], pinpointing the potential applicability of the developed formulations.

Future research directions will be oriented in order to tackle the following aspects: (i) a more comprehensive analysis of time-step and mesh size dependence in the dynamic regime, considering also different type of time integrators,

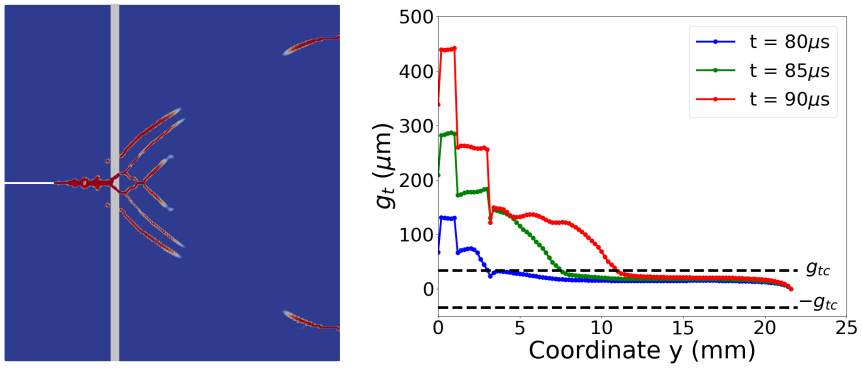

(a) (b)

Figure 16: Case 1 subjected to a strain rate of 1000 s^{-1}: (a) crack pattern; (b) tangential gaps along the interface for different time steps.

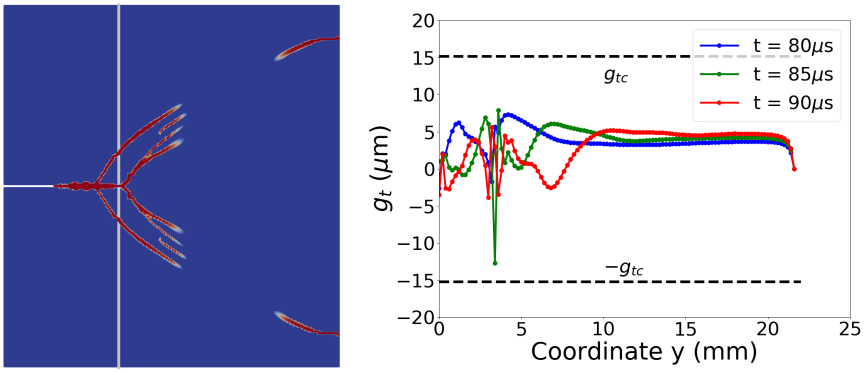

(a) (b)

Figure 17: Case 6 subjected to a strain rate of 1000 s^{-1}: (a) crack pattern; (b) tangential gaps along the interface for different time steps.

(ii) the consideration of more elaborated cohesive constitutive laws that account for gradual deterioration upon failure, (iii) extension to different interface thickness values and loading rates, (iv) conduction of experimental tests in order to provide a more thorough understanding of cracking behaviour of heterogeneous systems.

Data Availability

The processed data required to reproduce these findings available from the corresponding author on reasonable request.

CRediT authorship contribution statement

Mauro Corrado: Methodology, Investigation, Writing - original draft. **Marco Paggi**: Conceptualization, Supervision, Writing - review & editing. **José Reinoso**: Methodology, Software, Writing - original draft.

Declaration of Competing Interest

The authors declare that they have no known competing financial interests or personal relationships that could have appeared to influence the work reported in this paper.

Acknowledgments

MP acknowledges the support from the Italian Ministry of Education, University and Research (MIUR) to the research project of relevant national interest (PRIN 2017) "XFASTSIMS: Extra fast and accurate simulation of complex structural systems" (CUP: D68D19001260001).

References

References

[1] G. Francfort, J.-J. Marigo, Revisiting brittle fracture as an energy minimization problem, Journal of the Mechanics and Physics of Solids 46 (8) (1998) 1319 – 1342.

[2] B. Bourdin, G. A. Francfort, J.-J. Marigo, Numerical experiments in revisited brittle fracture, Journal of the Mechanics and Physics of Solids 48 (4) (2000) 797–826.

[3] E. Tanné, T. Li, B. Bourdin, J.-J. Marigo, C. Maurini, Crack nucleation in variational phase-field models of brittle fracture, Journal of the Mechanics and Physics of Solids 110 (2018) 80–99.

[4] C. Miehe, F. Welschinger, M. Hofacker, Thermodynamically consistent phase-field models of fracture: Variational principles and multi-field fe implementations, International Journal for Numerical Methods in Engineering 83 (10) (2010) 1273–1311.

[5] M. Ambati, T. Gerasimov, L. De Lorenzis, Phase-field modeling of ductile fracture, Computational Mechanics 55 (5) (2015) 1017–1040.

[6] F. Aldakheel, A microscale model for concrete failure in poro-elasto-plastic media, Theoretical and Applied Fracture Mechanics 107 (2020) 102517.

[7] E. Martínez-Pañeda, A. Golahmar, C. F. Niordson, A phase field formulation for hydrogen assisted cracking, Computer Methods in Applied Mechanics and Engineering 342 (2018) 742 – 761.

[8] T. Guillén-Hernández, I. G. García, J. Reinoso, M. Paggi, A micromechanical analysis of inter-fiber failure in long reinforced composites based on the phase field approach of fracture combined with the cohesive zone model, International Journal of Fracture (2019).

[9] V. Carollo, J. Reinoso, M. Paggi, A 3d finite strain model for intralayer and interlayer crack simulation coupling the phase field approach and cohesive zone model, Composite Structures 182 (2017) 636 – 651.

[10] M. Paggi, M. Corrado, J. Reinoso, Fracture of solar-grade anisotropic polycrystalline silicon: A combined phase field–cohesive zone model approach, Computer Methods in Applied Mechanics and Engineering 330 (2018) 123 – 148.

[11] J. Wu, A unified phase-field theory for the mechanics of damage and quasi-brittle failure, Journal of the Mechanics and Physics of Solids 103 (2017) 72–99.

[12] M. Hofacker, C. Miehe, Continuum phase field modeling of dynamic fracture: variational principles and staggered FE implementation, International Journal of Fracture 178 (2012) 113–129. doi:10.1007/s10704-012-9753-8.

[13] A. Schlüter, A. Willenbücher, C. Khun, R. Muller, Phase field approximation of dynamic brittle fracture, Computational Mechanics 54 (2014) 1141–1161. doi:10.1007/s00466-014-1045-x.

[14] M. J. Borden, C. V. Verhoosel, M. A. Scott, T. J. Hughes, C. M. Landis, A phase-field description of dynamic brittle fracture, Computer Methods in Applied Mechanics and Engineering 217-220 (2012) 77 – 95. doi:10.1016/j.cma.2012.01.008.

[15] T. Li, J.-J. Marigo, D. Guilbaud, S. Potapov, Gradient damage modeling of brittle fracture in an explicit dynamics context, International Journal for Numerical Methods in Engineering 108 (2016) 1381–1405.

[16] J. Bleyer, C. Roux-Langlois, J.-F. Molinari, Dynamic crack propagation with a variational phase-field model: limiting speed, crack branching and velocity-toughening mechanisms, International Journal of Fracture 204 (1) (2017) 79–100. doi:10.1007/s10704-016-0163-1.

[17] V. Nguyen, J.-Y. Wub, Modeling dynamic fracture of solids with a phase-field regularized cohesive zone model, Computer Methods in Applied Mechanics and Engineering 340 (2018) 1000–1022.

[18] M. Paggi, J. Reinoso, Revisiting the problem of a crack impinging on an interface: A modeling framework for the interaction between the phase field approach for brittle fracture and the interface cohesive zone model, Computer Methods in Applied Mechanics and Engineering 321 (2017) 145 – 172.

[19] M. Corrado, M. Paggi, Nonlinear fracture dynamics of laminates with finite

thickness adhesives, Mechanics of Materials 80 (2015) 183 – 192, materials and Interfaces. doi:10.1016/j.mechmat.2014.07.012.

[20] G. Mariggiò, J. Reinoso, M. Paggi, M. Corrado, Peeling of thick adhesive interfaces: The role of dynamics and geometrical nonlinearity, Mechanics Research Communications 94 (2018) 21 – 27.

[21] C. Miehe, M. Hofacker, F. Welschinger, A phase field model for rate-independent crack propagation: Robust algorithmic implementation based on operator splits, Computer Methods in Applied Mechanics and Engineering 199 (45-48) (2010) 2765–2778.

[22] B. Bourdin, G. A. Francfort, J.-J. Marigo, Numerical experiments in revisited brittle fracture, Journal of the Mechanics and Physics of Solids 48 (4) (2000) 797–826.

[23] O. Zienkiewicz, R. Taylor, The Finite Element Method: Solid Mechanics, Vol. 2, Butterworth-Heinemann, 2000.

[24] A. Ioannidou-Kati, M. Santarsiero, P. de Vries, S. Teixeira de Freitas, C. Louter, Mechanical behavior of transparent structural silicone adhesive (tssa) steel-to-glass laminated connections under monotonic and cyclic loading, Glass Structures and Engineering 3 (2018) 213–236.

[25] N. Stein, P. Weißgraeber, W. Becker, A model for brittle failure in adhesive lap joints of arbitrary joint configuration, Composite Structures 133 (2015) 707–718.

[26] P. Rosendahl, M. Drass, J. Schneider, W. Becker, Crack nucleation in hyperelastic adhesive bonds, in: Engineering Transparency 2018. Glass in Architecture and Structural Engineering, 2018, pp. 531–547.

[27] F. Zhou, J.-F. Molinari, T. Shioya, A rate-dependent cohesive model for simulating dynamic crack propagation in brittle materials, Engineering Fracture Mechanics 72 (9) (2005) 1383–1410.

[28] L. Xu, A. Rosakis, An experimental study of impact-induced failure events in homogeneous layered materials using dynamic photoelasticity and high-speed photography, Optic and Lasers in Engineering 40 (2003) 263–288.

[29] N. Parab, W. Chen, Crack propagation through interfaces in a borosilicate glass and a glass ceramic, International Journal of Applied Glass Science 5 (4) (2014) 353–362. doi:10.1111/ijag.12093.